A Field Camera for MR Sequence Monitoring and System Analysis

Benjamin E. Dietrich,[1] David O. Brunner,[1,2] Bertram J. Wilm,[1,2] Christoph Barmet,[1,2] Simon Gross,[1] Lars Kasper,[1,3] Maximilian Haeberlin,[1] Thomas Schmid,[1] S. Johanna Vannesjo,[1] and Klaas P. Pruessmann[1]*

Purpose: MR image formation and interpretation relies on highly accurate dynamic magnetic fields of high fidelity. A range of mechanisms still limit magnetic field fidelity, including magnet drifts, eddy currents, and finite linearity and stability of power amplifiers used to drive gradient and shim coils. Addressing remaining errors by means of hardware, sequence, or signal processing optimizations, calls for immediate observation by magnetic field monitoring. The present work presents a stand-alone monitoring system delivering insight into such field imperfections for MR sequence and system analysis.
Methods: A flexible NMR field probe-based stand-alone monitoring system, built on a software-defined-radio approach, is introduced and used to sense field dynamics up to third-order in space in a selection of situations with different time scales.
Results: Highly sensitive trajectories are measured and successfully used for image reconstruction. Further field perturbations due to mechanical oscillations and thermal field drifts following demanding gradient use and external interferences are studied.
Conclusion: A flexible and versatile monitoring system is presented, delivering camera-like access to otherwise hardly accessible field dynamics with nanotesla resolution. Its stand-alone nature enables field analysis even during unknown MR system states. **Magn Reson Med 75:1831–1840, 2016.** © 2015 Wiley Periodicals, Inc.

Key words: magnetic field monitoring; stand-alone; monitoring; hardware; field camera; gradients; trajectories; field drifts; gradient vibrations; scanner cool-down

INTRODUCTION

The accurate formation and interpretation of MR image data relies on static uniform and dynamic gradient fields of extreme fidelity. Consequently, the hardware used for generating these fields has seen continued engineering advances in the past and affords high degrees of field accuracy in present-day MRI systems. However, a range of confounding mechanisms still limit magnetic field fidelity. These include magnet drifts, eddy currents induced by the switching of gradient and shim fields (1), finite linearity and stability of amplifiers and supplies, mechanical resonances (2,3), and heating effects (4). At the image level, such field imperfections can impair results in various ways ranging from blurring and distortion to artefacts and signal dropouts.

Remaining field errors continue to be addressed at the hardware and sequence levels as well as by advances in signal processing and image reconstruction. All of these approaches require insight into the underlying imperfections, calling for immediate observation by magnetic field measurement. To serve the purpose, such measurements must be feasible in high background fields, offer high sensitivity and temporal resolution and should also capture the relevant spatial degrees of freedom of the magnetic field. It has been demonstrated that these requirements can be met by field sensors based on nuclear magnetic resonance (NMR) relying on the same basic physics as MRI itself (5–7). Pulsed NMR field measurement is based on the acquisition of free induction decay (FID) signals from small NMR-active samples. The phase of these FIDs directly reflects the integral of the magnetic field magnitude at the probe position. Using an array of spatially distributed probes permits expansion of these field integrals in terms of suitable spatial basis functions (8). Low-frequency (quasi-stationary) magnetic fields that originate outside a given volume of interest permit robust expansion based on field probes surrounding that volume using, e.g., spherical harmonics (8). The necessary spatial order of such expansion and hence the number of probes required depends on the proximity of relevant field sources relative to the diameter of the volume of interest. The field's temporal integral is most relevant for image reconstruction and considerations of k-space trajectories and image encoding. The field evolution per se is retrieved by temporal differentiation of the probe phase expansion.

Using the same physical principle as MRI, the implementation of NMR field sensing can partly rely on hardware and methods that are already available in MRI systems. Early implementations did so to a large degree, involving the host systems' entire transmit and receive chains, and incorporating field probe operation in pulse sequence programs (8,9). Yet the convenience of such close integration comes at the expense of flexibility, calling for greater independence from the MRI equipment

---

and procedures to be monitored. First steps in this direction have been the transitions to local probe transmitters (10) and heteronuclear field probes, relying on fluorine or other nonproton samples for spectral decoupling from imaging experiments (11–13). However, relying on the RF chains, spectrometer, and console of a host system still imposes major limitations and constraints, particularly in terms of sequencing options, measurement timing and bandwidth, data throughput, and receiver specifications. Taking up receiver channels for field monitoring also limits the performance of imaging experiments. Moreover, toward the implementation of a genuine measurement device (14) it is unsatisfactory that field sensing should require the system under test to be fully operational.

In the present work these limitations are overcome by the transition to a stand-alone device, which will be referred to as a field camera. The proposed system is designed to record spatiotemporal field evolutions up to third order in terms of spherical harmonics, relying on an array of 16 field probes as first proposed in Barmet et al (14). It is equipped with custom-designed RF chains including pulse synthesis, per-channel power amplification, transmit–receive (T/R)-switching, and two-stage amplification in the receive path. The camera's spectrometer is based on a software-defined-radio (SDR) design, using direct undersampling with high-rate analog-to-digital converters and signal manipulation mostly in the digital domain. The SDR approach simplifies the analog receive modules and adds flexibility to signal conditioning at the expense of large digital data flows (15). Parallel, real-time signal processing at suitable rates is accomplished with field programmable gate arrays (FPGA) before data output for higher-level processing, display and storage.

To illustrate the versatility and usefulness of the proposed camera system, field dynamics have been studied in a selection of situations involving different time scales. Measurement of k-space trajectories is illustrated by monitoring of echo-planar-imaging (EPI) readouts and use of the results for image reconstruction. Further examples demonstrate the observation of field perturbation due to mechanical oscillation of gradient coils, thermal field drift after demanding gradient use, and field errors induced by external sources such as trams passing near the laboratory.

METHODS

Hardware

The proposed system combines a field probe frontend with a transmit chain and a receive section based on a typical SDR approach with direct RF digitization. Figure 1a schematically illustrates the most important system components and their interconnections. The system consists of 4 main building blocks: A field probe array, first and second stage receive and excitation electronics, and a digitization/digital signal processing block. The first stage comprising T/R-switches and amplifiers is closely integrated with the camera head for placement in the scanner bore to avoid SNR loss in long cables. The sec-

ond stage and digital processing part are placed outside the high magnetic field due to the use of ferrite in baluns and power supplies.

Field Probe Array

The implemented field probe array is based on the probe design described in Refs. (10,14) and consists of 16 ^{1}H-based field probes built from 0.8 mm inner diameter glass capillaries filled with H_2O doped with $CuSO_4$. For each probe a five-turn solenoid serves as a T/R coil. The capillary is encased in an ellipsoidal, susceptibility-matched epoxy housing (5,14). The field probes are placed on the surface of a 17 cm diameter sphere using an approximately even distribution found by repulsive-potentials simulation. Figure 1a shows a schematic representation of the probe positions along with a close-up view of a probehead. Figure 1e shows a fully assembled field camera head. Figure 1f displays a packaged version with a custom-designed polyurethane housing including the first stage transmit and receive electronics.

Analog RF Chain

Each field sensor is connected to a T/R module (Fig. 1) consisting of a T/R-switch, an excitation power amplifier (PA), and a low-noise receive amplifier (LNA). Field effect transistor (FET)-based T/R-switches are used to achieve sub-microsecond switching performance. The more common option of PIN-diode switches exhibits better high-power signal compliance, but the required bias currents can sum up to a significant overall power consumption (16), which was avoided here to limit thermal changes in the measurement unit. Additional advantages of FET switches include integrated packaging and the fact that they do not require quarter-wavelength transformation, matching components, or high-current driver circuits. The noise figure of the T/R module, including T/R-switch and LNA, was determined at 0.9 dB. The 16 T/R-modules are connected to one motherboard responsible for supply, trigger, and excitation pulse distribution. All components of the first stage (T/R-switch, LNA, PA, and control logic) are placed within approximately 50 cm distance from the field sensors. This is a tradeoff between cable losses in front of the LNA that cannot be recovered, and field perturbations caused by the electronics. Care was taken to keep those to a minimum and at the same time protect the sensitive electronics from gradient-induced eddy currents, which would otherwise cause detrimental signal modulations.

A second stage of electronics as depicted in Figure 1 boosts and filters the receive signal such that it fits the ADC input range and prevents unintended aliasing. Digitally controllable attenuators and selectable amplifier bypasses enable gain scaling such that the ADC range can be used in an SNR-optimal way with different field probes. The resulting overall adjustable gain of the receive chain is −1.7–79.5 dB. Again, 16 gain-scaling and filtering modules are connected to one motherboard. A programmable direct digital synthesis (DDS) module generates frequency-modulated excitation pulses of variable duration (typically 2–8 µs). Active power splitters placed on the first-stage motherboard distribute these
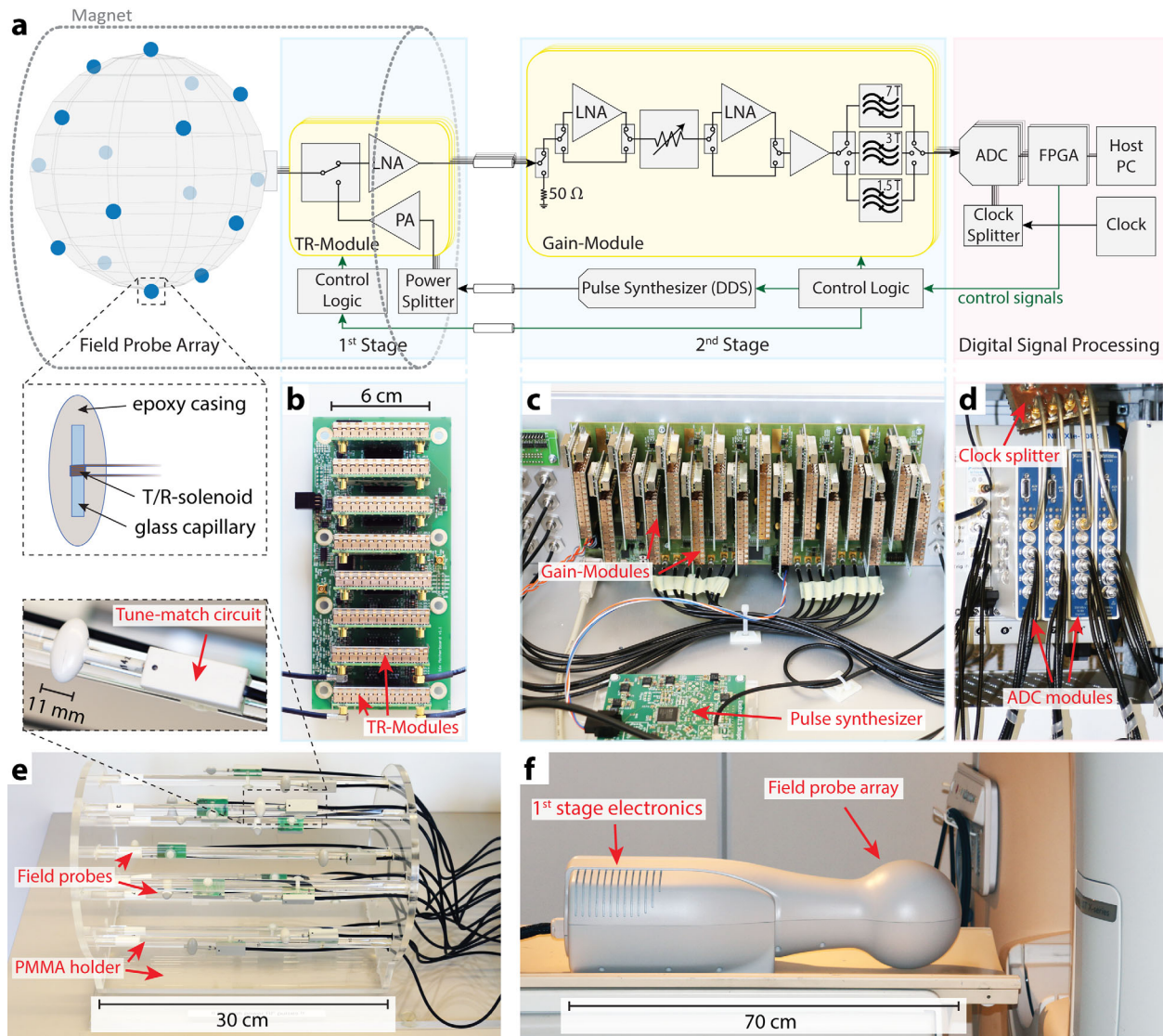
FIG. 1. **a**: stand-alone monitoring system schematic and its building blocks. From left to right: field probe array; 1st stage electronics typically placed inside the scanner bore, comprising transmit-receive-switches, low noise amplifiers, and excitation amplifiers; 2nd stage electronics comprising adjustable gain stage, anti-aliasing filters, and an excitation pulse generation module (DDS); and the digital signal processing stage consisting of digitizer modules, field programmable gate-array modules, and a processing and control computer. **b**: 1st stage electronics prototype. **c**: 2nd stage electronics. **d**: Digitizer modules. **e**: Assembled field camera head and close-up of a field probe. **f**: Packaged version including 1st-stage electronics, mounted in a polyurethane body.

pulses to all 16 transmit PAs, which can boost them to a maximum output power of 3 W per channel. The whole system, except for the tuned field probes and the anti-aliasing filter at the ADC input, supports a large bandwidth of 50–500 MHz and hence a wide range of field strengths and nuclei. The anti-aliasing filters can be selected through software from a set of filters, to fit the frequency range given by the magnet strength and monitoring nucleus. These settings can be different for different channels, permitting the simultaneous operation of field probes based on different nuclei.

Digitization/Decimation

Digitization and digital signal processing (digital signal processing stage in Figure 1) is based on National Instru-

ments (Austin, TX) hardware comprising NI 5761 14-bit ADCs sampling at 180–250 MHz, NI 7961R FPGA modules for real-time demodulation, filtering, and downsampling, and a host controller (NI 8133, NI 1082) for further signal processing, data visualization, sequence control, and data storage. Four channels are processed by each ADC and FPGA module resulting in a total maximum input data rate of 56 Gbit/s for 16 channels. Figure 2 depicts the implemented fixed-point I-Q demodulation, filter, and decimation chain composed of a shared DDS module for sine and cosine generation, high-speed multipliers, a cascade-integrate-comb (CIC) predecimation low-pass filter, and a finite-impulse-response (FIR) gaincompensation and decimation low-pass filter. The actual output data rate can be adjusted by means of the decimation rate and is typically set to 1 MHz (complex
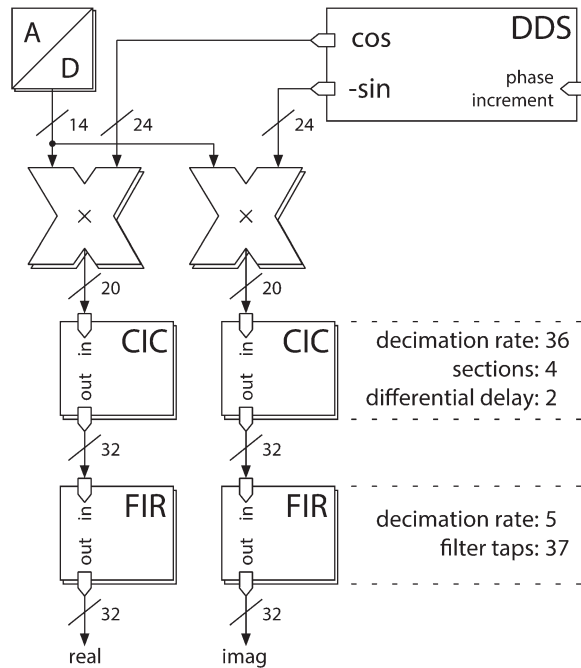
FIG. 2. Digital real-time processing implemented on the FPGA modules. The digitized signals from each channel (14 Bit) are multiplied with a sine and cosine and decimated through two filter stages, yielding the complex raw data signal with a real and imaginary word width of 32 Bit each. Specifications of the implemented filters for 128 MHz operation are indicated.

samples), which is amply sufficient for the gradient strengths of typical MRI systems.

The direct digitization approach simplifies the analog receiver design by removing the need for analog mixers, intermediate frequency filters, and potentially additional gain stages. Instead of a low phase-noise local oscillator for mixing a low phase-noise digitization clock is required and the sampling frequency needs to be carefully selected together with the ADC input anti-aliasing filter to prevent unintended signal aliases. Any jitter or drift of the sampling clock results in a measurement error of the uniform (B_0) field component. An NI 6674T timing and synchronization module is used to generate the digitization clock with a jitter of 230 fs (200 MHz carrier, 10 Hz to 1 MHz carrier offset phase noise integration range) based on a 50 ppb/year reference oscillator.

Timing

A set of pulse generators, implemented on one of the FPGA modules, serves as sequence controller and generates all required control signals. Each sequence is typically started/synchronized with an external trigger signal from the MR system under test, followed by a configurable series of probe excitation-acquisition periods. The sequence controller operates on a 100 MHz clock which is phase locked with the digitization reference clock. This results in a sequence timing and external trigger synchronization resolution of 10 ns, which is considered adequate for most field measurement scenarios, because gradient chains are typically limited to bandwidths below 50 kHz. Figure 3 depicts a typical sequence of
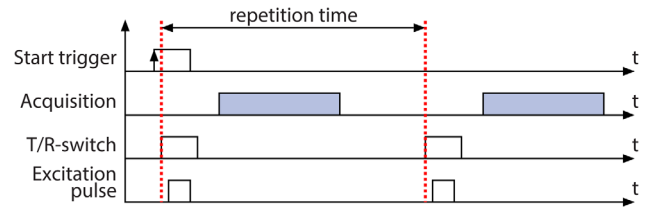

FIG. 3. Control signal timing of a typical monitoring sequence. An external trigger from the MR system under test starts the probe excitation-acquisition sequence.

control signals, excitation pulses and acquisition intervals.

To use field measurements for image reconstruction, a common time base needs to be established between the field camera and the MRI system, accounting for receive chain delays and different sampling rates. For this purpose the two systems are synchronized by locking the camera's reference oscillator onto the reference clock of the MRI system. Delay calibration was achieved with an amplitude-modulated test signal transmitted into both receive chains during a synchronization scan. The difference in sampling rate was corrected by resampling the measured k-space trajectory according to the typically lower bandwidth of the raw imaging data.

High-Level Signal Processing

Following low-level signal processing on the FPGAs as described above, higher-level processing is performed on the controller CPU. It comprises extraction of the phase of the probe signals, unwrapping, and fitting to a third-order, real-valued, spherical-harmonic field model (8). The resulting time-varying phase coefficients reflect the global phase term (k_0), the familiar k-space coordinates (k_x, k_y, k_z), as well as second, and third-order components. The temporal derivatives of the phase time courses represent the spatially uniform field component, the familiar gradient field evolutions (G_x, G_y, G_z), and higher-order field contributions. At the level of phase and field coefficients, further filtering and down sampling can be performed to reduce noise and data size. The choice of final bandwidth depends on the highest frequencies of field variation that occur in the given MRI system. In the present work, it was 50 kHz based on the observation that the gradient chains create the highest-frequency field dynamics.

Experiments

All measurements were performed in a whole-body Philips Achieva 3 Tesla (T) system (Philips Healthcare, Best, The Netherlands). Imaging experiments used a commercially available eight-channel head receive array.

Receive Chain Performance

The digitizer's signal-to-noise ratio (SNR), spur-free dynamic range (SFDR), and additive root-mean-square (RMS) phase jitter were measured using a reference signal from a SMA 100A signal generator (Rohde & Schwarz, Munich, Germany). The frequencies of the signal generator and receiver were set to 128 MHz, to simulate 3T ^{1}H operation. The resulting receiver output data

rate was set to 1 MHz. Using 100 ms acquisitions, the additive RMS phase jitter was calculated by integration of the phase noise spectrum starting at a carrier offset frequency of 10 Hz and subtracting the phase noise of the reference signal generator, which was measured with an NI PXI-5660 vector signal analyzer. Third-order inter-modulation distortion (IMD3) of the whole receive chain was measured by means of a two-tone measurement with a second signal generator (SMB 100A, Rohde & Schwarz, Munich, Germany). The second tone was set to a carrier offset frequency of 100 kHz. The two tones were fed into the T/R-module while the system was properly set up in the scanner bore at a combined signal level of -50 dBm, which is equivalent to the initial signal strength of a large (>2 mm diameter) field probe and hence represents a worst-case intermodulation condition.

Trajectory Measurement and Image Reconstruction

The basic functionality of determining field dynamics during challenging gradient sequences was explored in examples of single-shot EPI with uniform and variable speed (17) as well as an example of multiple-shot spiral scanning. The parameters of the uniform EPI readout were echo time (TE) = 25 ms, slice thickness = 2.5 mm, field of view (FOV) = 230 $\times$ 230 mm^2, resolution = 2.5 $\times$ 2.5 mm^2.

Table 1
Receiver Performance Results (128 MHz Operation)

SNR (1 MSPS)	82.2 dB
SFDR (1 MSPS)	96.7 dB
Additive RMS phase jitter of the digitizer (1 MSPS, 10 Hz offset)	230 fs
Third-order intermodulation distortion (IMD3)	74.7 dB
Noise figure 1. stage	0.9 dB
Gain 1. stage	22.1 dB
Noise figure 2. stage	2.3 dB
Gain 2. stage	$-23.8 - 57.4$ dB

The parameters of the variable-speed readout were TE = 35 ms, slice thickness = 1.8 mm, FOV 230 $\times$ 230 mm^2, resolution = 1.8 $\times$ 1.8 mm^2, SENSE factor 3. For the spiral scan the parameters were TE = 1.4 ms, repetition time (TR) = 1.6 s, slice thickness = 3 mm, FOV 228 $\times$ 228 mm^2, resolution = 1 $\times$ 1 mm^2, eight interleaves. To use measured k-space trajectories for image reconstruction, the camera measurement and the actual imaging procedure were performed in sequence, using synchronization as described above. B_0 and receive coil sensitivity maps were obtained with a common spin-warp gradient-echo sequence, performed with TE = 4.5 ms and TE = 6.8 ms and yielding 1 mm in-plane resolution. Image reconstruction was based on zeroth- and first-order results of the
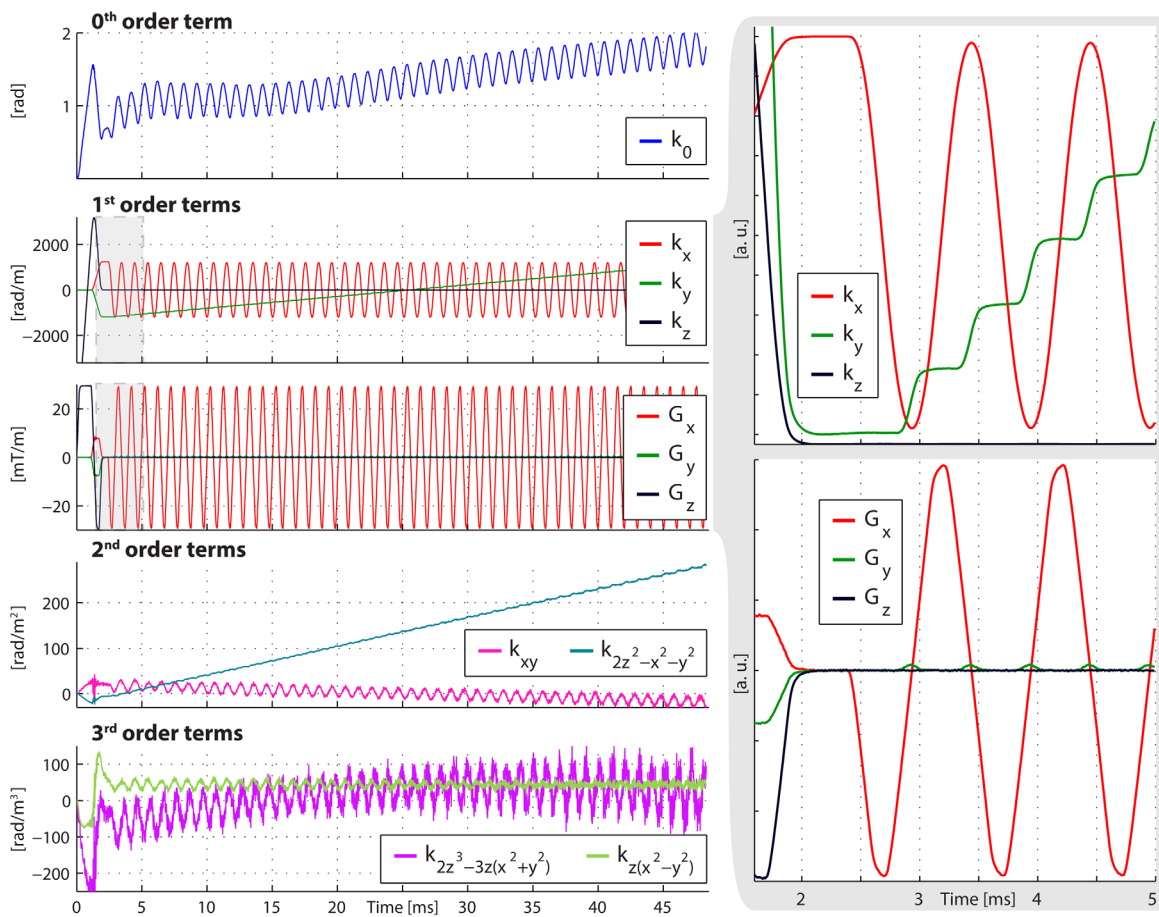

FIG. 4. Fully monitored 2.5 $\times$ 2.5 $\times$ 2.5 mm^3 voxel size, 230 $\times$ 230 mm^2 FOV, single shot EPI, including slice selection and re-phasing gradients. Selection of the calculated phase coefficients in time domain at a bandwidth of 50 kHz, and zoomed excerpt of the first order coefficients and derivatives (gradients).
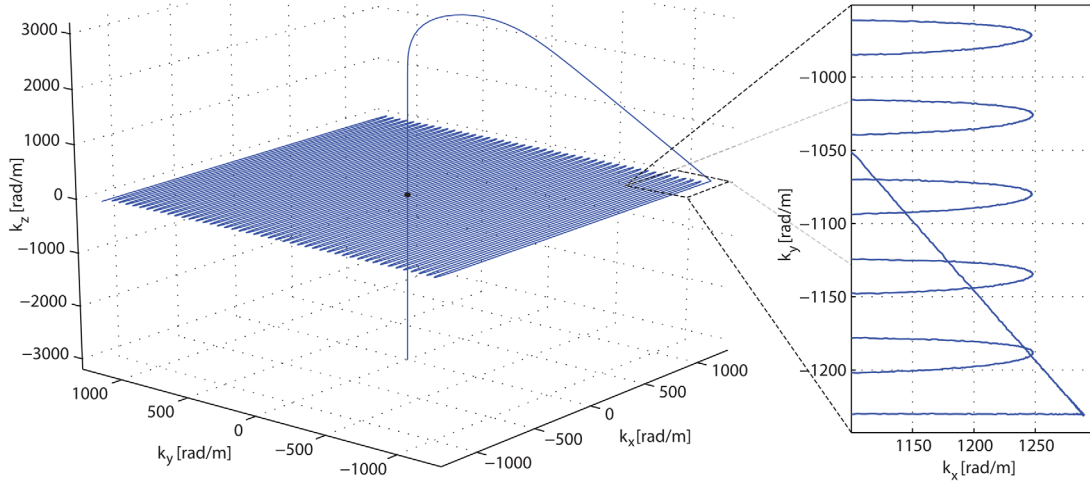
FIG. 5. The 3D k-space representation and zoomed excerpt at 1 MHz bandwidth of a fully monitored $2.5 \times 2.5 \times 2.5$ mm^3 voxel size, 230×230 mm^2 FOV, single shot EPI trajectory including slice selection and re-phasing.

field measurements as well as the B_0 and sensitivity maps, using iterative algebraic reconstruction as described in Kasper et al and Pruessmann et al (17,18).

Mechanical Vibrations

Field effects of mechanical gradient vibrations were examined in the following setting: Each gradient coil was separately driven to 35 mT/m for 100 ms and then switched off with the maximum slew rate, resulting in a steep, and approximately 200 μs long, gradient slope. The field camera was excited 70 μs before the slope onset to capture the switching event and ensuing field dynamics. Fields were studied in the time and frequency domains, including comparison with an acoustic spectrum obtained with a microphone.
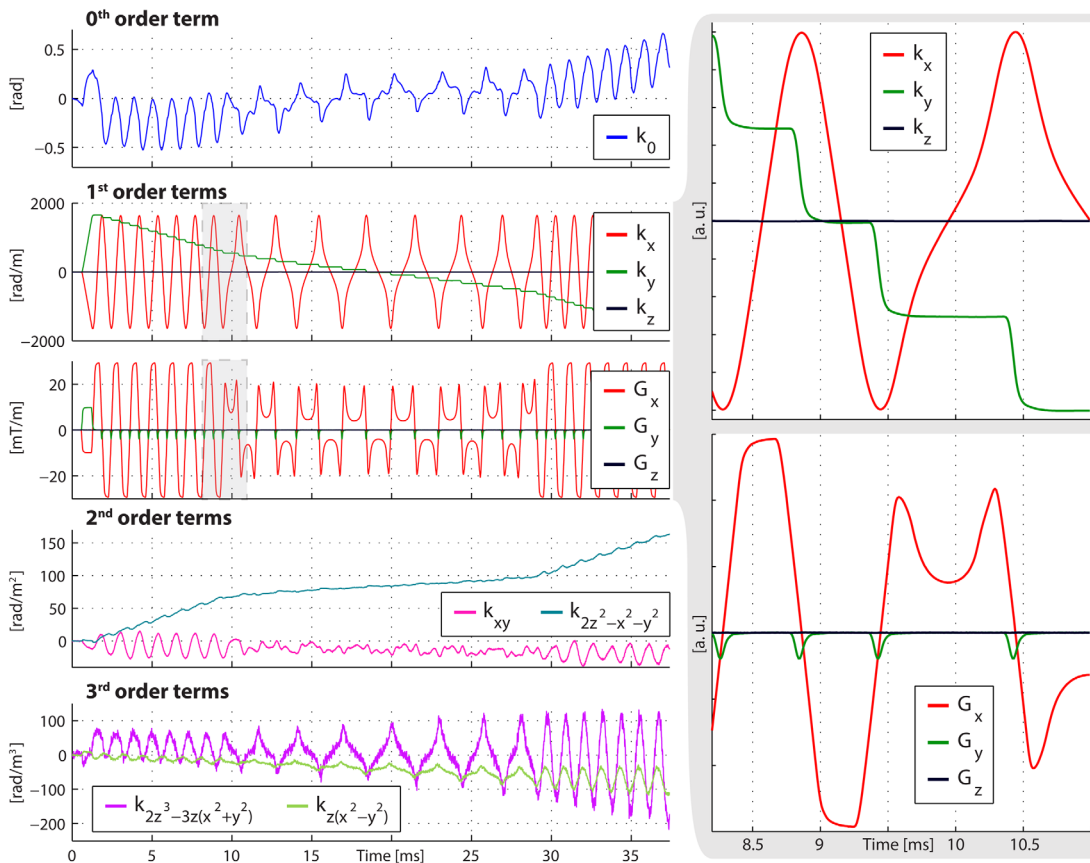

FIG. 6. Monitored variable density (matched-filter) EPI, phase coefficients, gradient waveforms and zoomed excerpts of the 1st order fields.

FIG. 7. One of the gradient echo images used for coil sensitivity and B_0 mapping (**a**), monitored 2D accelerated variable density EPI trajectory (**b**), and interleave of the monitored spiral trajectory (**c**). In vivo (**d**) and phantom (**e**) image reconstructed with the monitored variable density EPI trajectory, phantom image reconstructed with the monitored spiral trajectory (**f**), and images reconstructed with the corresponding nominal trajectories given by the sequence (**g–i**).
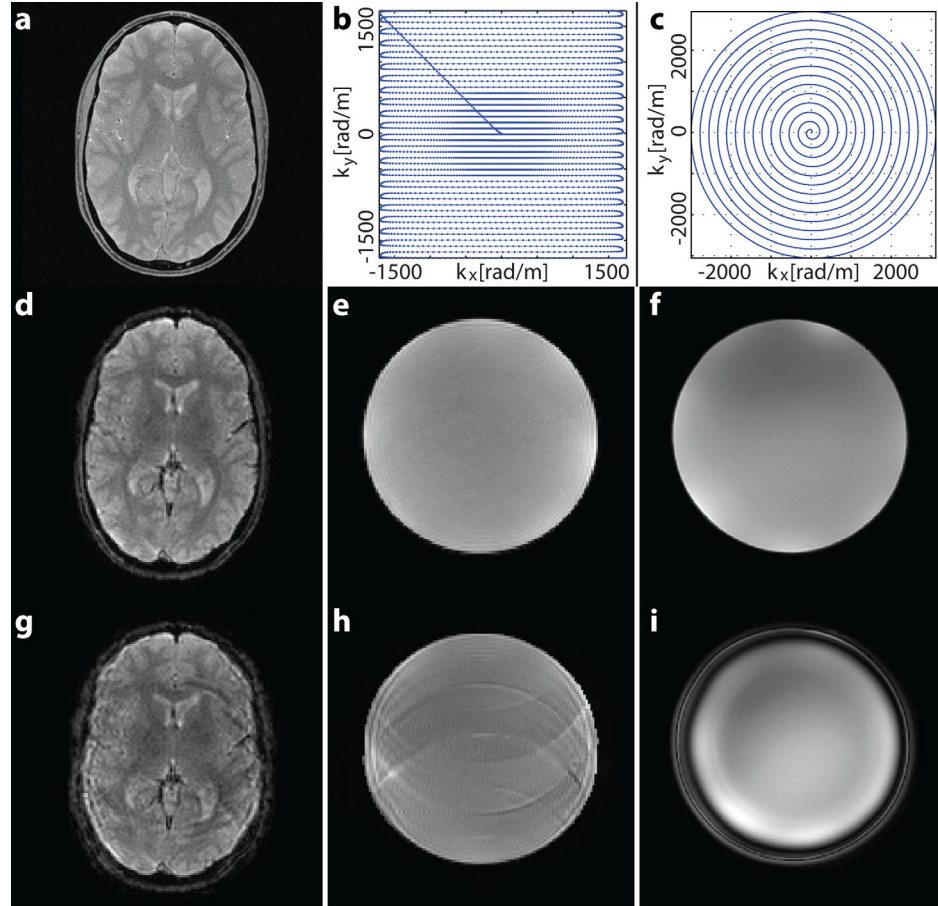
Field Drifts and External Perturbations

Field fluctuations and drifts were studied with the following protocol: Initially, an EPI readout sequence with high duty cycle was played out on the scanner after being idle for several hours. The imaging parameters were chosen to reflect typical values used in functional MRI (fMRI) as follows: two-dimensional (2D) single-shot gradient echo EPI with a TE of 35 ms, a FOV of 220 × 220 × 48 mm, 10 slices with an inter-slice gap of 2.5 mm, a voxel size of $2.6 \times 2.6 \times 2.5$ mm^3, 400 dynamics with a slice TR of 3 s, and sequence TR of 300 ms, resulting in a total of 4000 EPI readouts in 20 min. After the EPI protocol the subsequent magnetic field evolution in the idle scanner was observed for 120 min, with a temporal resolution of 595 ms. This was realized by repetitive probe excitation with each excitation-readout cycle yielding one data point. Field coefficients for each data point were obtained by linear regression of probe phase time courses of 150 ms and subsequent transform into the basis of spherical harmonics.

RESULTS

Table 1 shows the performance figures of the receiver module. The achieved probe sensitivity was assessed at $\xi = SNR\sqrt{BW} = 1.0 \times 10^5 \sqrt{Hz}$ (5), resulting in an initial SNR of 40 dB at an acquisition bandwidth of 1 MHz, which is well below the receiver SNR, rendering the sys-

tem probe-limited. Probe T_2^* was assessed as 65 ms. The maximum k-space range resulting from the probe droplet diameter of $d = 0.8$ *mm* was, according to Barmet et al (8),: $k_{max} = (2.86\ \pi)/d \approx 11231\ rad/m$.

Sequence Monitoring and Image Reconstruction

A fully monitored single-shot EPI trajectory, including slice-selection and re-phasing gradients, is shown in Figure 4. The scanner-independent operation enables monitoring even during slice excitation, when the scanner is in transmit mode and typically not capable of acquiring any signal. Monitoring the large moments of the slice-selection gradients challenges the probes almost up to their de-phasing limits, which can be seen in the increased noise at around 1.5 ms. The close-ups show typical smoothing effects of the bandwidth limitation of the gradient system. Figure 5 shows the corresponding measured 3D trajectory and excursions due to slice selection. A monitoring result for the case of variable-density EPI is shown in Figure 6. In both cases the dynamics of the zeroth-order (k_0) component relate to eddy currents, which can be concluded from their temporal relationship to gradient switching. The drifting second-order terms, illustrated by the blue graphs in Figures 4 and 6, most likely reflect concomitant-field effects, which depend on the squared magnitude of the readout gradient strength and hence drives over the whole readout into the same direction and has a smaller slope in the middle of the variable density EPI. The close-up in
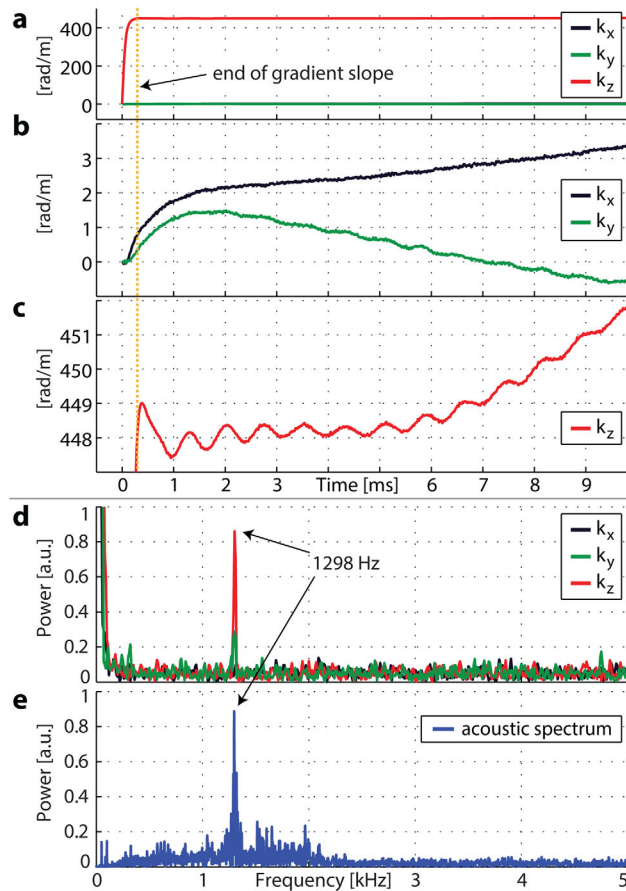
FIG. 8. Dynamics of the 1st order phase coefficients during and after a steep z-gradient slope (**a**: all 1st order coefficients, **b** and **c** zoomed), as well as corresponding frequency domain representation (**d**) and acoustic spectrum of a microphone (**e**).

Figure 6 nicely shows that the EPI blips end up having a tail due to the finite bandwidth of the gradient system's impulse response function. This is less critical in the imaging case because its integral and hence the distance between adjacent k-space lines is more important than the exact shape of the curve. Corresponding 2D trajectory, phantom and in vivo images based on the measured variable-density trajectory, as well as spiral trajectories are shown in Figure 7. The absence of perceivable ghosting and blurring in Figures 7d, e, and f demonstrates consistency between the monitored trajectories and imaging data. Figures 7g–i show corresponding images reconstructed using nominal trajectories. Figure 7a shows one of the gradient echo images used for coil sensitivity and B_0 mapping, again reconstructed on the monitored trajectory.

Mechanical Vibrations

Figure 8 shows time evolutions and corresponding frequency domain components of the first order phase coefficients during and following a steep gradient turn-off event. The zoomed plot (Fig. 8c) of k_z shows a distinct oscillation at 1298 kHz with an amplitude of approximately 0.75 rad/m and a decay time of approximately 15 ms, while the other coefficients (Fig. 8b) appear to be mostly affected by rather slow eddy currents. A compari-

son with the acoustic spectrum (Figures 8d,e) confirms the mechanical nature of the observed oscillation.

Field Drifts/Fluctuations

Intensive gradient duty cycles heat-up the scanner, which can cause field drifts. Figure 9 shows the field evolution of an idle scanner over a period of 2 h right after a demanding fMRI scan session. Several effects can be observed, such as disabling of the shim system at around 2 min, a B_0 drift with a decay constant of approximately 15 min, fluctuations due to the cryogenic pump, fluctuations due to trams passing close to the MR system site, a repeatable change in almost all field orders at around 94 min, and many more. The effect of the cryogenic pump is mostly visible in the B_0 and G_y terms, where it appears like an increased noise level. The power spectrum of the B_0 term in Figure 9b reveals an alias of the pumps' primary acoustic frequency component, which cannot directly be resolved due to the limited time resolution of 595 ms. Shortening this time is possible but can lead, given the relaxation times of the used field probes, to spurious echo formation. A rather regular pattern of disturbances following roughly the 7 min schedule of the public transport system can be seen in the first and second-order terms. The B_0 term does not show these disturbances, which is most likely due to the shielding effect of the super-conducting magnet. The 94 min glitch is most likely due to a change in the operation mode of the scanner, such as shutdown of the gradient cooling system.

The measured field noise (Fig. 9) is in the range of 2.5 nT for the zeroth, 7.5 nT/m for the first, 19.3 nT/m² for the second, and 124 nT/m³ for the third order terms (averaged over all components of each order). The field measurement sensitivity of the probe array can be calculated by extending the thermal noise based field sensitivity approximation from (5) (Eq. [10]) with the noise propagation due to the spatial field-model from (8) (Eq. [8]) yielding: $\sigma_{B_l} \approx \frac{\sqrt{6}}{\gamma \xi T_{obs}^{3/2}} \sqrt{\sum_j \left(P_{l,j}^+ \right)^2}$. In other words, the probe phase noise is scaled by the magnitude of the corresponding row of the pseudo-inverse of the probing matrix, which reflects the probe position calibration in terms of the used basis functions. This results using an observation time of 150 ms - in 2.6 pT for the zeroth, 55 pT/m for the first, 1.3 nT/m² for the second, and 20 nT/m³ for the third-order terms. The same calculation based on the sensitivity due to the additive jitter of the receiver (Table 1) gives 68 fT for the zeroth, 1.4 pT/m for the first, 33 pT/m² for the second, and 543 pT/m³ for the third-order terms. The measured noise is hence roughly 3 orders of magnitude higher than the theoretical sensitivity, which is also roughly 3 orders of magnitude higher than the noise due to the receiver. This suggests that the measurement is field noise limited.

DISCUSSION

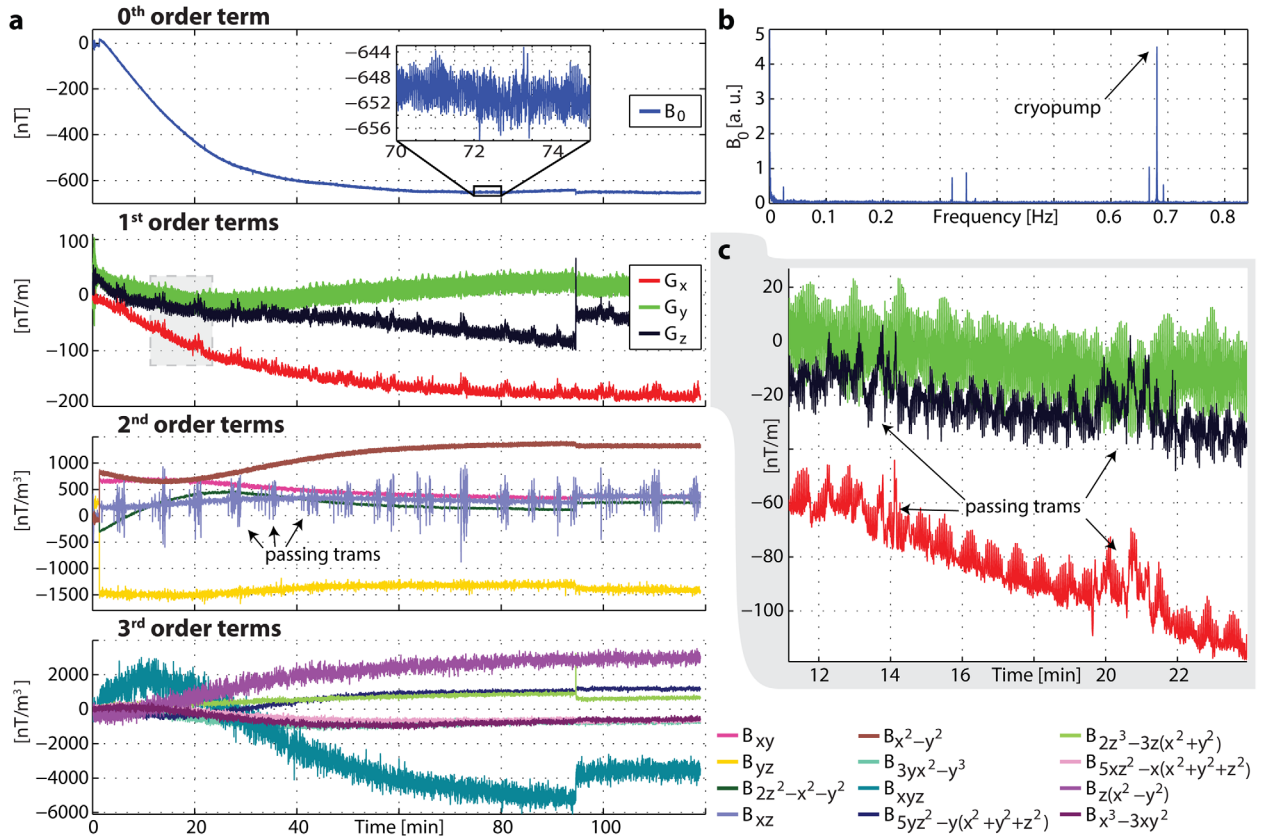This work reports the implementation of a stand-alone system for dynamic magnetic field monitoring,

FIG. 9. Field evolution of the idle scanner over a period of 120 min, starting right after a 20 min fMRI scan (**a**). Power spectrum of the 0th order component (**b**), and zoomed excerpt of the 1st order components time evolution (**c**).

delivering camera-like access to field dynamics in MR systems with high temporal resolution and sensitivity in the nanotesla range. The implemented system was evaluated at 3 T, delivering insights into otherwise poorly accessible field dynamics such as slice excitation, effects of mechanical vibrations, eddy currents, and magnet cool-down. The accuracy of the monitored trajectories proved suitable for challenging variable density EPI image reconstructions.

The current implementation permits real-time field monitoring and visualization up to a duty cycle of 25% with a probe re-excitation period of roughly 600 ms, given the relaxation times of the used field probes ($T_2^* \approx 65\ ms$) and a very conservative level of accepted spurious coherences from previous excitations.

A comparison of measured field noise with the theoretical values based on the sensitivity of the probes and the receiver revealed that the measurements are limited by actual field noise.

Because the field probes measure the magnitude of the magnetic field, it is expected that the derived spatial field distributions deviate from the main magnet axis due to concomitant fields of the gradient system. This is typically not a problem because the imaging sample is also subject to these deviations. If required, this could be circumvented by an increased number of probes and optimized basis functions for concomitant fields, as well as an optimized spatial probe positioning. Another

approach could be analytical calculation of the expected concomitant fields and retrospective correction of the phase evolutions.

Direct sampling and FPGA-based real-time data processing render the proposed system flexible and easily adjustable to different requirements. Scalability in terms of number of channels, support for different scanner vendors, field strength, and nuclei, is designed into the modular receive, excitation, and data processing chains. Filters and bandwidth can be changed without hardware modifications, and processing steps can be moved to the FPGAs to increase performance for real-time field monitoring applications. Its flexible nature, ability to acquire data with a duty cycle of up to 100% over arbitrary durations, only limited by the hard disk size, its real-time field data processing capabilities, modular interfaces, and scalable design, make it useful for a whole range of other applications such as impulse response based gradient and shim system characterization (19,20). In conjunction with a switch to another nucleus, the system can be transformed from a pure analysis and characterization instrument into an active field controller for real-time field stabilization, as has been shown by Duerst et al and Wilm et al (21,22). A whole range of other applications might profit from these capabilities, for example field probe based motion correction (23) or other concurrent monitoring and imaging modalities (24).

REFERENCES

1. Boesch C, Gruetter R, Martin E. Temporal and spatial analysis of fields generated by eddy currents in superconducting magnets. Magn Reson Med 1991;20:268–284.
2. Barnett A. Comments on "Gradient-induced acoustic and magnetic field fluctuations in a 4T whole-body MR imager". Magn Reson Med 2001;46:207.
3. Nixon TW, McIntyre S, Rothman DL, de Graaf, Robin A. Compensation of gradient-induced magnetic field perturbations. J Magn Reson 2008;192:209–217.
4. Ebel A, Maudsley AA. Detection and correction of frequency instabilities for volumetric 1H echo-planar spectroscopic imaging. Magn Reson Med 2005;53:465–469
5. Zanche ND, Barmet C, Nordmeyer-Massner JA, Pruessmann KP. NMR probes for measuring magnetic fields and field dynamics in MR systems. Magn Reson Med 2008;60:176–186.
6. Pound R, Knight W. A radiofrequency spectrograph and simple magnetic-field meter. Rev Sci Instrum 1950;21:219–225.
7. Boero G, Frounchi J, Furrer B, Besse PA, Popovic RS. Fully integrated probe for proton nuclear magnetic resonance magnetometry. Rev Sci Instrum 2001;72:2764–2768.
8. Barmet C, Zanche ND, Pruessmann KP. Spatiotemporal magnetic field monitoring for MR. Magn Reson Med 2008;60:187–197.
9. Han H, MacGregor RP, Balcom BJ. Pure phase encode magnetic field gradient monitor. J Magn Reson 2009;201:212–217.
10. Barmet C, Zanche ND, Wilm BJ, Pruessmann KP. A transmit/receive system for magnetic field monitoring of in vivo MRI. Magn Reson Med 2009;62:269–276.
11. Barmet C, Wilm BJ, Pavan M, Katsikatsos G, Keupp J, Mens G, Pruessmann KP. Concurrent higher-order field monitoring for routine head MRI: an integrated heteronuclear setup. In Proceedings of the Joint Annual Meeting of ISMRM-ESMRMB, Stockholm, Sweden, 2010. Abstract 216.
12. Wilm BJ, Barmet C, Pavan M, Pruessmann KP. Higher order reconstruction for MRI in the presence of spatiotemporal field perturbations. Magn Reson Med 2011;65:1690–1701.
13. Sipilä P, Greding S, Wachutka G, Wiesinger F. 2H Transmit-Receive NMR probes for magnetic field monitoring in MRI. Magn Reson Med 2011;65:1498–1506.
14. Barmet C, Wilm BJ, Pavan M, Pruessmann KP. A third-order field camera with microsecond resolution for MR system diagnostics. In Proceedings of the Annual Meeting of ISMRM, Honolulu, Hawaii, USA, 2009. Abstract 781.
15. Kenington PB. RF and baseband techniques for software defined radio. Boston: Artech House; 2005. xiii, 332.
16. Doherty Jr WE, Joos R. PIN diode circuit designers handbook. Watertown, MA: Microsemi Corporation; 1999.
17. Kasper L, Haeberlin M, Dietrich BE et al. Matched-filter acquisition for BOLD fMRI. Neuroimage. 2014;100C:145–160.
18. Pruessmann KP, Weiger M, Börnert P, Boesiger P. Advances in sensitivity encoding with arbitrary k-space trajectories. Magn Reson Med 2001;46:638–651.
19. Vannesjo SJ, Haeberlin M, Kasper L, Pavan M, Wilm BJ, Barmet C, Pruessmann KP. Gradient system characterization by impulse response measurements with a dynamic field camera. Magn Reson Med 2013;69:583–593.
20. Vannesjo SJ, Dietrich BE, Pavan M, Brunner DO, Wilm BJ, Barmet C, Pruessmann KP. Field camera measurements of gradient and shim impulse responses using frequency sweeps. Magn Reson Med 2014: 72:570–583.
21. Duerst Y, Wilm BJ, Dietrich BE, Vannesjo SJ, Barmet C, Schmid T, Brunner DO, Pruessmann KP. Real-time feedback for spatiotemporal field stabilization in MR systems. Magn Reson Med 2015:73:884–893.
22. Wilm BJ, Duerst Y, Dietrich BE, Wyss M, Vannesjo SJ, Schmid T, Brunner DO, Barmet C, Pruessmann KP. Feedback field control improves linewidths in in vivo magnetic resonance spectroscopy. Magn Reson Med 2014;71:1657–1662.
23. Haeberlin M, Kasper L, Barmet C, Brunner DO, Dietrich BE, Gross S, Wilm BJ, Kozerke S, Pruessmann KP. Real-time motion correction using gradient tones and head-mounted NMR field probes. Magn Reson Med 2015;74:647–660.
24. Vannesjo SJ, Wilm BJ, Duerst Y, Gross S, Brunner DO, Dietrich BE, Schmid T, Barmet C, Pruessmann KP. Retrospective correction of physiological field fluctuations in high-field brain MRI using concurrent field monitoring. Magn Reson Med 2015;73:1833–1843.